Letter

Formation of collisionless shocks driven by strongly magnetized relativistic electrons in the laboratory

P. T. Campbell,[1,*] B. K. Russell,[1,†] C. Dong,[2,3] G. Fiksel,[1] P. M. Nilson,[4] A. G. R. Thomas,[1] C. A. Walsh,[5] K. M. Krushelnick,[1] and L. Willingale[1]

[1]*Gérard Mourou Center for Ultrafast Optical Science, University of Michigan, 2200 Bonisteel Boulevard, Ann Arbor, Michigan 48109, USA*
[2]*Department of Astronomy, Boston University, Boston, Massachusetts 02215, USA*
[3]*Princeton Plasma Physics Laboratory and Department of Astrophysical Sciences, Princeton University, Princeton, New Jersey 08540, USA*
[4]*Laboratory for Laser Energetics, University of Rochester, 250 East River Road, Rochester, New York 14623, USA*
[5]*Lawrence Livermore National Laboratory, 7000 East Avenue, Livermore, California 94550, USA*

(Received 27 January 2023; revised 13 October 2023; accepted 15 December 2023; published 18 January 2024)

In experiments performed with the OMEGA EP laser system, proton deflectometry captured magnetic field dynamics consistent with collisionless shock formation driven by strongly magnetized relativistic electrons. During laser-foil interactions, shocks can form as relativistic electrons and strong surface magnetic fields generated by a short-pulse laser impinge on a cooler plasma produced by a longer-pulse laser. Three-dimensional particle-in-cell simulations reproduce the magnetic draping and fast formation speeds measured in the experiment and reveal that this relativistic-electron-driven shock forms at an interface that is unstable to shear and streaming instabilities. The simulation results provide insight into the microphysics that may influence high-energy shocks observed in extreme astrophysical environments.

DOI: 10.1103/PhysRevResearch.6.L012016

Collisionless shocks are a ubiquitous feature of many astrophysical systems that act to rapidly change the plasma properties in response to perturbations that move faster than characteristic speeds (e.g., sound speed, Alfvén speed). They form on a wide range of scales from the relatively low-energy bow shock ahead of Earth's magnetosphere with average upstream velocities of $v_{\rm us} \sim 450$ km/s [1], to the high-energy relativistic shocks ($v_{\rm us} \to c$) in pulsar wind nebulae (PWNe) [2]. While Earth's bow shock can be measured *in situ* by satellites [3], most astrophysical shocks can only be observed through spectral signatures radiated from distant objects. Modeling these systems is challenging due to the large scale of the shocks relative to the microphysics governing formation and evolution. Therefore, numerical studies are often limited to small-scale idealized simulations. Laboratory experiments can provide a rigorous method of exploring the microphysics of astrophysical systems and can provide insight into phenomena that cannot be resolved via *in situ* measurements as they are often taken at limited points along the trajectories of orbits. In addition, experiments that create energetic conditions can provide crucial benchmarking for the simulation tools typically applied to extreme astrophysics.

High-power lasers can drive shocks in high-energy-density conditions with a broad range of applications, including ion beam acceleration [4,5], compression of materials [6], and laboratory studies of the underlying mechanisms governing astrophysical shock formation and particle acceleration [7–10]. To date, experiments motivated by astrophysical shocks have focused on the nonrelativistic regime.

In the highest-energy astrophysical systems, including active galactic nuclei jets, gamma-ray bursts, and PWNe, relativistic inflow velocities are expected [11]. Additionally, shock formation can occur in the presence of extreme magnetic fields, as in PWNe where the electron cyclotron frequency ω_{ce} can exceed the electron plasma frequency ω_{pe}, $\sigma_{{\rm cold},e} = \omega_{ce}^2/\omega_{pe}^2 = B^2/\mu_0\gamma_0 m_e n_e c^2 > 1$ [12]. Several theoretical and computational studies have been performed in the astrophysics community for $\sigma \geqslant 0.1$ [13–16]. However, laboratory exploration of shock formation in relativistic plasma conditions has thus far been limited to ion acceleration by laser-driven electrostatic shocks [5,17].

In this Letter, two laser pulses with very different intensities and durations established plasma conditions for collisionless shock formation driven by highly magnetized ($\sigma_{{\rm cold},e} > 1$) relativistic electrons. A schematic of the experimental setup at the OMEGA EP laser facility is shown in Fig. 1.

First, a long-pulse laser (LP, nanosecond duration) is focused to a moderate intensity ($I_{\rm LP} \sim 10^{14}$ W cm^{-2}, in an 819-μm spot) onto a 50-μm-thick plastic (CH) or 25-μm-thick copper foil target. As the laser pulse ablates the surface, perpendicular temperature and density gradients in the plasma plume spontaneously generate an azimuthal magnetic field $\mathcal{O}$(MG) via the Biermann battery mechanism ($\frac{\partial B}{\partial t} = \frac{k_B}{en_e}\nabla T_e \times$

*campbpt@umich.edu
†bkruss@umich.edu

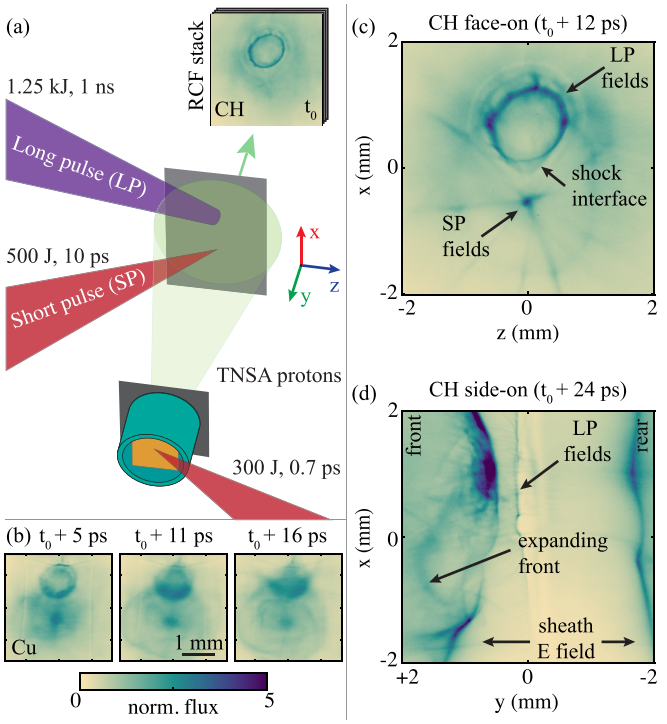

FIG. 1. (a) Schematic of the experimental setup. The high-intensity SP laser arrives at the main target at $t = t_0$ (after the LP-produced magnetic fields had already evolved for 750 ps). The overlaid image representing the radiochromic film (RCF) stack shows the magnetic field conditions at t_0. (b) A time series of proton images using a Cu target show the fast field dynamics on picosecond timescales. Snapshots from face-on and side-on imaging of the interaction with a CH target are annotated in (c) and (d), respectively. Axes are scaled by the probing magnification.

∇n_e) [18,19]. The self-generated magnetic field expands radially with a velocity near the plasma sound speed ($v \sim 10^5$–10^6 m/s) [20,21]. Nernst advection confines the fields to the high-density plasma near the target surface where the plasma pressure dominates the magnetic pressure [$\beta = nk_BT/(B^2/2\mu_0) \sim 1$–$100$] [22–24].

After the LP-produced plasma has evolved for 750 ps, a short-pulse (SP) laser is focused to high intensity [$a_0 \approx \sqrt{I\lambda_{\mu m}^2/1.4 \times 10^{18}(\mathrm{W\,cm^{-2}\,\mu m^2})} \approx 6$] onto the same target with a focal spot center-to-center separation of 1.25 mm. At these intensities, the laser accelerates electrons within the focal volume to relativistic velocities. The rapid expansion of a relativistic surface current establishes a target-normal sheath electric field [25] and generates an azimuthal magnetic field surrounding the focal spot. The magnetic field generated by the SP can be orders of magnitude stronger than the Biermann fields in the LP-produced plasma $\mathcal{O}(100\ \mathrm{MG})$ [26,27]. Indeed, the SP magnetic fields can be so strong that the magnetic energy density exceeds the energy density of the plasma electrons ($\sigma_{\mathrm{cold},e} > 1$). Previous experiments have applied these fields to study magnetic reconnection [28–30]. Here, the neighboring LP-produced plasma is effectively a quasistatic obstacle to the flow of relativistic electrons and the associated magnetic field.

Proton deflectometry captured the ultrafast magnetic field dynamics and images were recorded on radiochromic film (RCF) stacks. Key experimental results are summarized by snapshots in Figs. 1(b)–1(d). Included in Fig. 1(a) (representing the RCF stack) is a proton image of the undisturbed Biermann battery fields at the onset time of SP-driven fields, $t = t_0$. At this time, the LP-produced plasma has already evolved for 750 ps and the self-generated Biermann battery magnetic fields deflect protons inward to create a ring-shaped feature of proton accumulation.

Features associated with the SP evolve over picosecond timescales. Figure 1(b) shows a time series of proton images from a single shot with a copper target in the face-on probing geometry (illustrated by the setup schematic). As described in Sarri *et al.* [27], the SP-driven fields produce a central spot surrounded by an expanding ring in the proton image. This is evidence of a competition between the focusing magnetic field orientation generated on the front-surface (spot) and defocusing orientation on the rear-surface fields (ring). While the rear fields do not directly interact with the LP-produced plasma, the ring feature helps delineate the extent of the relativistic electron flows which sweep across both surfaces with similar speeds [26,27]. Consistent with Ref. [27], tracking the ring-feature expansion yields an estimated initial flow velocity of $\sim 0.5c$, which slows to $\sim 0.1c$ as the ring reaches a radius exceeding 1 mm.

After $t_0 + 5$ ps, the two plasmas collide and a conelike feature develops at the interface as the SP fields are driven into the Biermann battery fields. Note that the image resolution for the shot with a copper foil is degraded due to probe proton scattering in the target. In addition, the image contrast is impacted by a nonuniform background signal of protons emitted by the main target itself. As shown in Fig. 1(c), using a CH foil for the main target improved the image resolution. This enabled further analysis of the magnetic field profiles (summarized in Fig. 2). The face-on images of the CH foil also exhibit spokelike features in the SP fields likely caused by azimuthal perturbations due to the resistive filamentation instability in the cold and dense parts of the insulating target [31] (this effect is not considered in the forward modeling of the field dynamics shown in Fig. 2).

In Fig. 1(d), the probing geometry was rotated 90° to enable side-on imaging of similar times during the system evolution. This measurement is most sensitive to the sheath electric fields generated by target charging during the SP interaction. Nevertheless, the proton images also capture the disruption of the sheath field at the interface, as well as evidence of an expanding front moving back away from the interface ($-\hat{x}$ direction) at later times. A description of the probing geometry and a full time series of side-on images is included in the Supplemental Material [32].

To elucidate the magnetic field dynamics measured in the face-on geometry, a forward modeling method was employed (the Supplemental Material contains additional details [32]). For each time slice in Fig. 2(a), the panel is split to compare experimental data (left half) with synthetic proton images generated using analytic expressions to describe the magnetic fields. Key features of the experimental proton images can be reproduced, including the cone feature at the discontinuity between the two plasmas. Figure 2(b) shows the horizontal

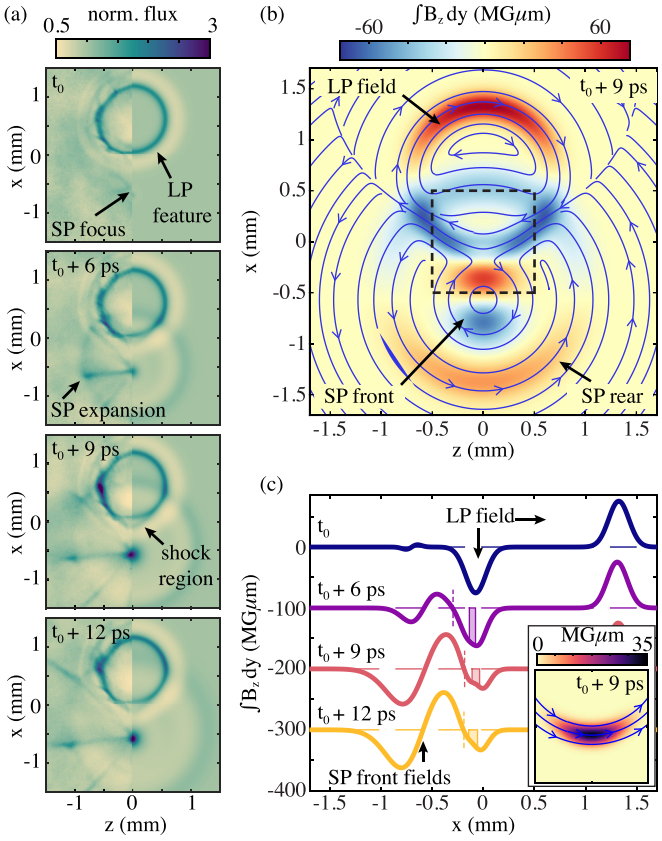

FIG. 2. (a) A time series of experimental proton images (left half of each time slice) from a single shot with a CH foil are compared to corresponding forward modeling results (right half). (b) An example field map from the forward modeling analysis for $t = t_0 + 9$ ps. Streamlines of a path-integrated magnetic field are overlaid on a map of the horizontal field component. (c) Lineouts taken at $z = 0$ from the field profiles for each time slice in (a) demonstrate the ultrafast temporal evolution of the magnetic fields and the modulation of the LP-produced Biermann fields at the interface. Rear-surface fields are excluded from (c) to emphasize the front-surface dynamics. Dashed vertical lines indicate the zero-crossing point between the SP- and LP-produced fields. Shaded areas show the modulated field region caused by the draped magnetic fields at the discontinuity. The inset plot in (c) shows an isolated 2D view of the draped magnetic field feature from the dashed box region in (b).

component of the path-integrated field profile at $t_0 + 9$ ps. The LP-produced Biermann battery fields are located in the upper half of the image, and the path-integrated field strength is consistent with previous experimental measurements [33]. The fields associated with the SP expand from the lower half of the target into the LP plasma obstacle. While the path-integrated amplitudes appear similar between the LP- and SP-produced fields, the SP fields are generated in a thin layer along the surface ($\Delta y_{SP} \ll \Delta y_{LP}$), and the fields are significantly stronger ($B_{SP} > 10B_{LP}$). The narrow spot feature caused by the front surface SP-produced fields may indicate caustic formation or proton trajectory crossing. Although the forward modeling method can reproduce the amplitude and width of the spot without any trajectory crossing, the result may still underestimate the peak SP-produced field strength.

Lineouts plotted in Fig. 2(c) show the temporal evolution of the interacting fields (excluding rear-surface fields for clarity). Over the picosecond timescale, the SP fields grow and expand, driving modulation and reduction of the path-integrated Biermann magnetic field at the interface. An isolated two-dimensional (2D) projection of the field feature required to reproduce the conelike modulation [inset in Fig. 2(c)] suggests a pileup and draping of SP-driven magnetic fields at the interface and formation of a tangential discontinuity. The projected discontinuity region thickness is 70–90 μm along the $\hat{x}$ direction, which is comparable to the ion skin depth (d_i), where $d_i = c/\omega_{pi} \sim 10$–$100$ μm along the LP-produced plasma plume [estimated from extended-magnetohydrodynamics (MHD) simulations, and comparable to values listed in Ref. [34]]. This measurement represents an upper bound, and the region may be thinner if the interface is tilted with respect to the proton probing path.

The field dynamics yielding the conelike feature evolve over supersonic and super-Alfvénic timescales with respect to LP-produced plasma. The zero-crossing point between the SP- and LP-produced fields [marked with vertical dashed lines in Fig. 2(c)] moves with $v \sim 0.1c$, similar to the SP-field expansion speed. The modulation caused by pileup at the tangential discontinuity develops over 6–9 ps, giving an estimated formation speed of 0.8–1.2×10^7 m/s [based on the region width described above and shown as shaded areas in Fig. 2(c)]. Both are fast compared to the characteristic LP Alfvén speed $v_A = 5 \times 10^4$ m/s and sound speed $c_s = 2 \times 10^5$ m/s, calculated for fully ionized CH ions using nominal values of $B_{LP} = 1$ MG, $T_e = 1$ keV, and $n_e = Zn_i = 1 \times 10^{21}$ cm^{-3} (the critical density for the SP laser frequency). The uncertainty in characterizing speeds is due to the ∼3 ps temporal spacing between RCF layers. After ∼10 ps, features in the face-on probing results are quasistatic, however, the side-on probing captures late-time expansion from the discontinuity region.

While face-on proton imaging is typically most sensitive to magnetic fields [35], the observed features may also correspond to electric fields generated at the discontinuity. The forward modeling interpretation is informed by simulations (discussed below) that predict a pileup and draping of magnetic fields at a tangential discontinuity, driving the formation of a collisionless shock that propagates into the LP-generated plume. The simulations also show electric fields that would contribute to the formation of the modulation. By attributing all deflections to the magnetic fields, the forward modeling results give an upper bound for the path-integrated magnetic field.

The thin discontinuity region ($\delta_x \leqslant d_i$) indicates that electron-scale physics could influence the dynamics below the spatial resolution of the proton source (∼15 μm). In addition, the proton images are path-integrated measurements. Information about fast dynamics driven by relativistic electrons could be lost during the relatively slow transit of protons across the fields, or due to the intrinsic ∼ps temporal resolution.

To study the details of the relativistic electron-driven microphysics, a reduced scale 3D simulation was performed using the fully relativistic particle-in-cell (PIC) code OSIRIS 4.0 [36,37]. A convergence tested, full-scale 3D PIC simulation of the interaction with box dimensions $\mathcal{O}$(mm) and time

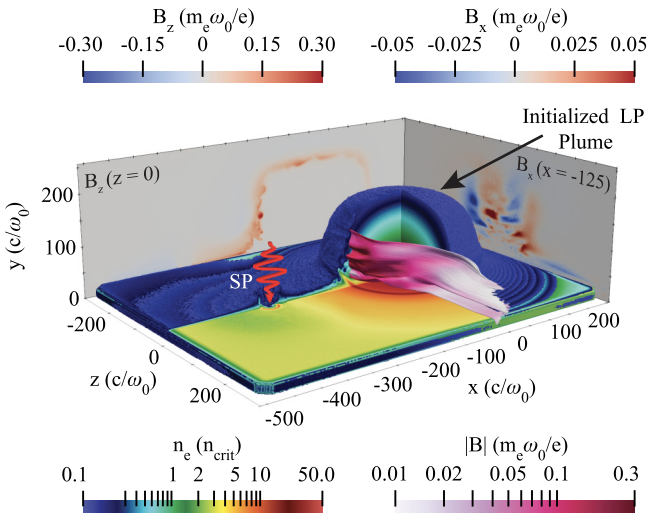

FIG. 3. A 3D surface of electron density at $t = 2667\omega_0^{-1}$ is plotted with a cutout to show SP-driven magnetic field lines draped around the LP plume. The fields are highly perturbed due to the unstable interface which results in strong regions of B_z (slice plotted on the $-z$ wall) and complex structures in B_x (slice on the $+x$ wall).

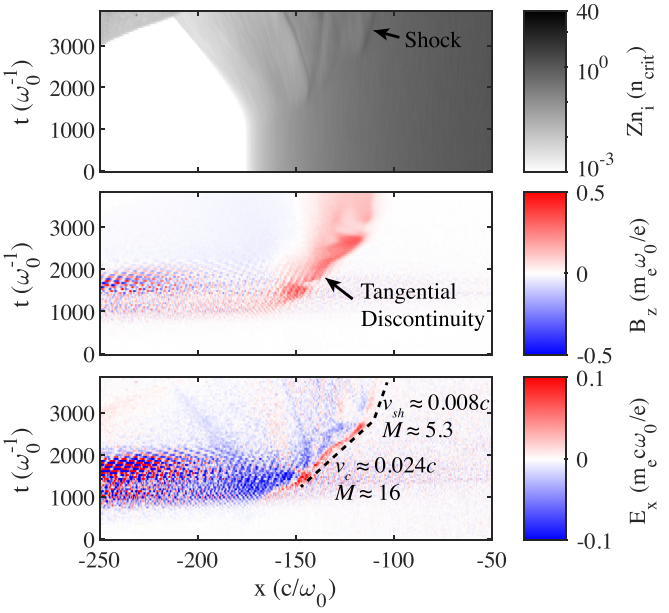

FIG. 4. Lineouts are taken from the 3D simulation at $y \approx 95(c/\omega_0)$, $z = 0$ at several time steps to form space-time plots of ion charge density Zn_i, magnetic field B_z, and electric field E_x. Lines are plotted over the electric field that follow the initial compression and late-time shock propagation with velocities v_c and v_{sh} and sonic Mach number M shown beside the respective lines. See Supplemental Fig. 2 for 2D slices of ion charge density showing the shock structure [32].

duration $\mathcal{O}$(ns) is not possible on currently available supercomputers, therefore several simplifications were made. The LP-generated plasma plume was initialized in OSIRIS based on fits to extended-MHD simulation results at $t = 750$ ps. The peak magnetic field strength, temperature, and density of the LP-generated plume near the interaction region were maintained to preserve β, but the spatial scale and SP duration were reduced by 25 times. Collisions were neglected because the electron-ion collision time predicted by the extended-MHD model was comparable to the entire PIC simulation time $\mathcal{O}$(1–10 ps).

The SP was injected from the positive y boundary and focused to $a_0 = 5$ on a target consisting of electrons and fully ionized carbon. The simulated temporal and spatial scales are normalized by the SP laser frequency ω_0. The particle density is normalized to the SP critical density (n_{crit}). Additional details about the simulation setup can be found in the Supplemental Material [32].

Consistent with the experimental measurements, strong SP-driven magnetic fields [$\sim$0.3 ($m_e\omega_0/e$) or 3 kT) initially expand radially at $\sim$0.2–0.4c. Magnetic field streamlines plotted with a 3D surface of electron density in Fig. 3 show how the fields drape after the magnetized relativistic electrons flow against the LP-produced plume. The draped fields are highly perturbed, or rippled, due to interfacial instabilities between the SP-driven electrons and LP-produced plume. The cold electron magnetization parameter $\sigma_{\text{cold},e}$ varies in the draped region (downstream side of the shock) with values exceeding 1 in regions of strong magnetic field.

Slices of B_z and B_x plotted on the figure walls demonstrate how the instabilities influence the magnetic field configuration, including producing regions of high magnetic flux (B_z) perpendicular to the shock direction ($+\hat{x}$). The instabilities form on electron kinetic scales and are likely driven by large velocity shear as SP-driven electrons flow up the face of the LP plume, creating conditions that are unstable to the magnetized electron-scale Kelvin-Helmholtz instability and the lower-hybrid drift instability [38,39]. Although not resolved in the presented proton deflectometry, the instabilities will be the subject of future work.

In Fig. 4, a time series of lineouts taken at $y \approx 95(c/\omega_0)$ and $z = 0$ are plotted for the ion charge density (Zn_i), perpendicular magnetic field (B_z), and shock-normal electric field (E_x). At $t \approx 1000(c/\omega_0)$, the magnetic field begins to pile up at a tangential discontinuity that travels a velocity of $\sim$0.024c in the $+x$ direction. For $t \gtrsim 2800\omega_0^{-1}$ the compression slows to $\sim$0.008c and a density jump is formed in both the electron and ion densities. The downstream-to-upstream electron density ratio is small, $\Gamma \sim 1.2$–1.4. A temperature ratio of $\Theta \sim$ 2–3 is also seen in the electrons with an upstream temperature of $\sim$3–4 keV. This gives a sound speed $c_s \approx 4.5 \times 10^5$ m/s corresponding to approximate sonic Mach numbers of 16 and 5.3 for the compression and shock speed, respectively. The downstream is small at the end of the simulation time, therefore these downstream values have been taken near the peak of the density jump. The maximum Mach number for these conditions can be calculated using Eq. (3) reported by Sorasio *et al.* [40]. This gives $M_{\text{max}} \sim 4.6$–6 which is consistent with the simulated shock Mach number. Additionally, the initial compression velocity is similar to the modulation formation speed estimated from the experimental proton images.

At late times, the unstable interface begins to decompress, and there is a backward ($-\hat{x}$) expansion of magnetic field and electric field. This effect likely produces the

backward propagating feature observed in the side-on proton images labeled "expanding front" in Fig. 1(d). In general, the simulations predict similar dynamics to the experimental measurements despite the reduced spatiotemporal scales, including reasonable agreement on the speed of field evolution in the discontinuity region.

This work demonstrates that collisionless shocks driven by strongly magnetized relativistic electrons can be created in the laboratory. The experiment captured ultrafast magnetic field dynamics consistent with shock formation. Large-scale PIC simulations elucidate how this laser-driven platform can produce shocks in conditions relevant to extreme astrophysical environments. As *in situ* measurements are currently unattainable, laboratory experiments can provide critical insights into the microphysics of such shocks. Future experiments may focus on the electron-scale instabilities at the tangential discontinuity, using fast optical probes to measure the instabilities and a modified experimental setup that aids in generating and diagnosing the instabilities. Plasma instabilities driven by shear flows are expected to play an important role in energy dissipation and particle acceleration in relativistic jets found around active galactic nuclei or gamma ray bursts [41]. Next-generation ultraintense laser facilities may also extend this experimental platform to much more energetic interactions where inflowing particle energies and fields are larger and quantum electrodynamics processes may become important to shock physics.

The data that support the findings of this Letter are available from the corresponding author upon reasonable request.

The authors would like to acknowledge useful discussions with Anatoly Spitkovsky. This material is based upon work supported by the Department of Energy National Nuclear Security Administration under Awards No. DE-NA0003606 and No. DE-NA0003954. B.K.R. is supported by the National Science Foundation through Award No. 1751462. C.D. was supported by the U.S. Department of Energy Early Career Research Award No. DE-SC0024639 and NASA Grant No. 80NSSC21K1326. The experiment was conducted at the Omega Laser Facility with the beam time through the National Laser Users' Facility (NLUF) (or the Laboratory Basic Science) under the auspices of the U.S. DOE/NNSA by the University of Rochester's Laboratory for Laser Energetics under Contract No. DE-NA0003856. The authors acknowledge the OSIRIS Consortium, consisting of UCLA and IST (Portugal) for the use of the OSIRIS 4.0 framework. Resources for this work were provided by the NASA High-End Computing (HEC) Program through the NASA Advanced Supercomputing (NAS) Division at Ames Research Center.

P.T.C. and B.K.R. contributed equally to this work.

[1] T. I. Gombosi, *Physics of the Space Environment* (Cambridge University Press, Cambridge, UK, 2004).

[2] B. M. Gaensler, S. Chatterjee, P. O. Slane, E. van der Swaluw, F. Camilo, and J. P. Hughes, The x-ray structure of the pulsar bow shock G189.22+2.90 in the supernova remnant IC 443, Astrophys. J. **648**, 1037 (2006).

[3] K. W. Behannon, Mapping of the Earth's bow shock and magnetic tail by Explorer 33, J. Geophys. Res. **73**, 907 (1968).

[4] L. O. Silva, M. Marti, J. R. Davies, R. A. Fonseca, C. Ren, F. S. Tsung, and W. B. Mori, Proton shock acceleration in laser-plasma interactions, Phys. Rev. Lett. **92**, 015002 (2004).

[5] D. Haberberger, S. Tochitsky, F. Fiuza, C. Gong, R. A. Fonseca, L. O. Silva, W. B. Mori, and C. Joshi, Collisionless shocks in laser-produced plasma generate monoenergetic high-energy proton beams, Nat. Phys. **8**, 95 (2012).

[6] D. Kraus, A. Ravasio, M. Gauthier, D. O. Gericke, J. Vorberger, S. Frydrych, J. Helfrich, L. B. Fletcher, G. Schaumann, B. Nagler, B. Barbrel, B. Bachmann, E. J. Gamboa, S. Göde, E. Granados, G. Gregori, H. J. Lee, P. Neumayer, W. Schumaker, T. Döppner, R. W. Falcone, S. H. Glenzer, and M. Roth, Nanosecond formation of diamond and lonsdaleite by shock compression of graphite, Nat. Commun. **7**, 10970 (2016).

[7] C. M. Huntington, F. Fiuza, J. S. Ross, A. B. Zylstra, R. P. Drake, D. H. Froula, G. Gregori, N. L. Kugland, C. C. Kuranz, M. C. Levy, C. K. Li, J. Meinecke, T. Morita, R. Petrasso, C. Plechaty, B. A. Remington, D. D. Ryutov, Y. Sakawa, A. Spitkovsky, H. Takabe, and H.-S. Park, Observation of magnetic field generation via the Weibel instability in interpenetrating plasma flows, Nat. Phys. **11**, 173 (2015).

[8] D. B. Schaeffer, W. Fox, D. Haberberger, G. Fiksel, A. Bhattacharjee, D. H. Barnak, S. X. Hu, and K. Germaschewski, Generation and evolution of high-Mach-number laser-driven magnetized collisionless shocks in the laboratory, Phys. Rev. Lett. **119**, 025001 (2017).

[9] A. Rigby, F. Cruz, B. Albertazzi, R. Bamford, A. R. Bell, J. E. Cross, F. Fraschetti, P. Graham, Y. Hara, P. M. Kozlowski, Y. Kuramitsu, D. Q. Lamb, S. Lebedev, J. R. Marques, F. Miniati, T. Morita, M. Oliver, B. Reville, Y. Sakawa, S. Sarkar, C. Spindloe, R. Trines, P. Tzeferacos, L. O. Silva, R. Bingham, M. Koenig, and G. Gregori, Electron acceleration by wave turbulence in a magnetized plasma, Nat. Phys. **14**, 475 (2018).

[10] F. Fiuza, G. F. Swadling, A. Grassi, H. G. Rinderknecht, D. P. Higginson, D. D. Ryutov, C. Bruulsema, R. P. Drake, S. Funk, S. Glenzer, G. Gregori, C. K. Li, B. B. Pollock, B. A. Remington, J. S. Ross, W. Rozmus, Y. Sakawa, A. Spitkovsky, S. Wilks, and H.-S. Park, Electron acceleration in laboratory-produced turbulent collisionless shocks, Nat. Phys. **16**, 916 (2020).

[11] L. Sironi, U. Keshet, and M. Lemoine, Relativistic shocks: Particle acceleration and magnetization, Space Sci. Rev. **191**, 519 (2015).

[12] L. Sironi and A. Spitkovsky, Acceleration of particles at the termination shock of a relativistic striped wind, Astrophys. J. **741**, 39 (2011).

[13] A. Spitkovsky, Simulations of relativistic collisionless shocks: Shock structure and particle acceleration, AIP Conf. Proc. **801**, 345 (2005).

[14] M. V. Barkov, M. Lyutikov, and D. Khangulyan, 3D dynamics and morphology of bow-shock pulsar wind nebulae, Mon. Not. R. Astron. Soc. **484**, 4760 (2019).

[15] L. Sironi, I. Plotnikov, J. Nättilä, and A. M. Beloborodov, Coherent electromagnetic emission from relativistic magnetized shocks, Phys. Rev. Lett. **127**, 035101 (2021).

[16] C. Demidem, J. Nättilä, and A. Veledina, Relativistic collisionless shocks in inhomogeneous magnetized plasmas, Astrophys. J. Lett. **947**, L10 (2023).

[17] M. S. Wei, S. P. D. Mangles, Z. Najmudin, B. Walton, A. Gopal, M. Tatarakis, A. E. Dangor, E. L. Clark, R. G. Evans, S. Fritzler, R. J. Clarke, C. Hernandez-Gomez, D. Neely, W. Mori, M. Tzoufras, and K. Krushelnick, Ion acceleration by collisionless shocks in high-intensity-laser–underdense-plasma interaction, Phys. Rev. Lett. **93**, 155003 (2004).

[18] L. Biermann and A. Schlüter, Cosmic radiation and cosmic magnetic fields. II. Origin of cosmic magnetic fields, Phys. Rev. **82**, 863 (1951).

[19] J. A. Stamper and B. H. Ripin, Faraday-rotation measurements of megagauss magnetic fields in laser-produced plasmas, Phys. Rev. Lett. **34**, 138 (1975).

[20] L. Gao, P. M. Nilson, I. V. Igumenshchev, M. G. Haines, D. H. Froula, R. Betti, and D. D. Meyerhofer, Precision mapping of laser-driven magnetic fields and their evolution in high-energy-density plasmas, Phys. Rev. Lett. **114**, 215003 (2015).

[21] P. T. Campbell, C. A. Walsh, B. K. Russell, J. P. Chittenden, A. Crilly, G. Fiksel, L. Gao, I. V. Igumenshchev, P. M. Nilson, A. G. R. Thomas, K. Krushelnick, and L. Willingale, Measuring magnetic flux suppression in high-power laser–plasma interactions, Phys. Plasmas **29**, 012701 (2022).

[22] M. G. Haines, Heat flux effects in Ohm's law, Plasma Phys. Controlled Fusion **28**, 1705 (1986).

[23] L. Willingale, A. G. R. Thomas, P. M. Nilson, M. C. Kaluza, S. Bandyopadhyay, A. E. Dangor, R. G. Evans, P. Fernandes, M. G. Haines, C. Kamperidis *et al.*, Fast advection of magnetic fields by hot electrons, Phys. Rev. Lett. **105**, 095001 (2010).

[24] L. Lancia, B. Albertazzi, C. Boniface, A. Grisollet, R. Riquier, F. Chaland, K.-C. Le Thanh, P. Mellor, P. Antici, S. Buffechoux *et al.*, Topology of megagauss magnetic fields and of heat-carrying electrons produced in a high-power laser-solid interaction, Phys. Rev. Lett. **113**, 235001 (2014).

[25] S. C. Wilks, A. B. Langdon, T. E. Cowan, M. Roth, M. Singh, S. Hatchett, M. H. Key, D. Pennington, A. MacKinnon, and R. A. Snavely, Energetic proton generation in ultra-intense laser–solid interactions, Phys. Plasmas **8**, 542 (2001).

[26] W. Schumaker, N. Nakanii, C. McGuffey, C. Zulick, V. Chyvkov, F. Dollar, H. Habara, G. Kalintchenko, A. Maksimchuk, K. A. Tanaka, A. G. R. Thomas, V. Yanovsky, and K. Krushelnick, Ultrafast electron radiography of magnetic fields in high-intensity laser-solid interactions, Phys. Rev. Lett. **110**, 015003 (2013).

[27] G. Sarri, A. Macchi, C. A. Cecchetti, S. Kar, T. V. Liseykina, X. H. Yang, M. E. Dieckmann, J. Fuchs, M. Galimberti, L. A. Gizzi *et al.*, Dynamics of self-generated, large amplitude magnetic fields following high-intensity laser matter interaction, Phys. Rev. Lett. **109**, 205002 (2012).

[28] A. E. Raymond, C. F. Dong, A. McKelvey, C. Zulick, N. Alexander, A. Bhattacharjee, P. T. Campbell, H. Chen, V. Chvykov, E. Del Rio, P. Fitzsimmons, W. Fox, B. Hou, A. Maksimchuk, C. Mileham, J. Nees, P. M. Nilson, C. Stoeckl, A. G. R. Thomas, M. S. Wei, V. Yanovsky, K. Krushelnick, and L. Willingale, Relativistic-electron-driven magnetic reconnection in the laboratory, Phys. Rev. E **98**, 043207 (2018).

[29] C. A. J. Palmer, P. T. Campbell, Y. Ma, L. Antonelli, A. F. A. Bott, G. Gregori, J. Halliday, Y. Katzir, P. Kordell, K. Krushelnick, S. V. Lebedev, E. Montgomery, M. Notley, D. C. Carroll, C. P. Ridgers, A. A. Schekochihin, M. J. V. Streeter, A. G. R. Thomas, E. R. Tubman, N. Woolsey, and L. Willingale, Field reconstruction from proton radiography of intense laser driven magnetic reconnection, Phys. Plasmas **26**, 083109 (2019).

[30] K. F. F. Law, Y. Abe, A. Morace, Y. Arikawa, S. Sakata, S. Lee, K. Matsuo, H. Morita, Y. Ochiai, C. Liu, A. Yogo, K. Okamoto, D. Golovin, M. Ehret, T. Ozaki, M. Nakai, Y. Sentoku, J. J. Santos, E. d'Humières, P. Korneev, and S. Fujioka, Relativistic magnetic reconnection in laser laboratory for testing an emission mechanism of hard-state black hole system, Phys. Rev. E **102**, 033202 (2020).

[31] C. Ruyer, S. Bolaños, B. Albertazzi, S. N. Chen, P. Antici, J. Böker, V. Dervieux, L. Lancia, M. Nakatsutsumi, L. Romagnani, R. Shepherd, M. Swantusch, M. Borghesi, O. Willi, H. Pépin, M. Starodubtsev, M. Grech, C. Riconda, L. Gremillet, and J. Fuchs, Growth of concomitant laser-driven collisionless and resistive electron filamentation instabilities over large spatiotemporal scales, Nat. Phys. **16**, 983 (2020).

[32] See Supplemental Material at http://link.aps.org/supplemental/10.1103/PhysRevResearch.6.L012016 for a description of the proton deflectometry analysis and additional experimental and simulation data.

[33] P. T. Campbell, C. A. Walsh, B. K. Russell, J. P. Chittenden, A. Crilly, G. Fiksel, P. M. Nilson, A. G. R. Thomas, K. Krushelnick, and L. Willingale, Magnetic signatures of radiation-driven double ablation fronts, Phys. Rev. Lett. **125**, 145001 (2020).

[34] W. Fox, A. Bhattacharjee, and K. Germaschewski, Magnetic reconnection in high-energy-density laser-produced plasmas, Phys. Plasmas **19**, 056309 (2012).

[35] C. K. Li, F. H. Séguin, J. A. Frenje, J. R. Rygg, R. D. Petrasso, R. P. J. Town, P. A. Amendt, S. P. Hatchett, O. L. Landen, A. J. Mackinnon, P. K. Patel, V. A. Smalyuk, T. C. Sangster, and J. P. Knauer, Measuring E and B fields in laser-produced plasmas with monoenergetic proton radiography, Phys. Rev. Lett. **97**, 135003 (2006).

[36] R. A. Fonseca, L. O. Silva, F. S. Tsung, V. K. Decyk, W. Lu, C. Ren, W. B. Mori, S. Deng, S. Lee, T. Katsouleas, and J. C. Adam, OSIRIS: A three-dimensional, fully relativistic particle in cell code for modeling plasma based accelerators, in *Computational Science — ICCS 2002*, edited by P. M. A. Sloot, A. G. Hoekstra, C. J. K. Tan, and J. J. Dongarra (Springer, Berlin, 2002), pp. 342–351.

[37] R. G. Hemker, Particle-in-cell modeling of plasma-based accelerators in two and three dimensions, arXiv:1503.00276.

[38] J. Dargent, F. Lavorenti, F. Califano, P. Henri, F. Pucci, and S. S. Cerri, Interplay between Kelvin–Helmholtz and lower-hybrid drift instabilities, J. Plasma Phys. **85**, 805850601 (2019).

[39] E. P. Alves, T. Grismayer, R. A. Fonseca, and L. O. Silva, Electron-scale shear instabilities: Magnetic field generation and

particle acceleration in astrophysical jets, New J. Phys. **16**, 035007 (2014).

[40] G. Sorasio, M. Marti, R. Fonseca, and L. O. Silva, Very high Mach-number electrostatic shocks in collisionless plasmas, Phys. Rev. Lett. **96**, 045005 (2006).

[41] E. P. Alves, T. Grismayer, S. F. Martins, F. Fiúza, R. A. Fonseca, and L. O. Silva, Large-scale magnetic field generation via the kinetic Kelvin–Helmholtz instability in unmagnetized scenarios, Astrophys. J. **746**, L14 (2012).